# A torsional MRE joint for a C-shaped robotic leg



2017 Smart Mater. Struct. 26 015002

(http://iopscience.iop.org/0964-1726/26/1/015002)

IOP Publishing Smart Materials and Structures
Smart Mater. Struct. 26 (2017) 015002 (10pp) doi:10.1088/0964-1726/26/1/015002

# A torsional MRE joint for a C-shaped robotic leg

M D Christie[1], S S Sun[1], D H Ning[2], H Du[2], S W Zhang[3,4] and W H Li[1,4]

[1] School of Mechanical, Materials and Mechatronic Engineering, University of Wollongong, New South Wales 2522, Australia
[2] School of Electrical, Computer & Telecommunications Engineering, University of Wollongong, New South Wales 2522, Australia
[3] Department of Precision Machinery and Precision Instrumentation, University of Science and Technology of China, Hefei, Anhui province 230026, People's Republic of China

E-mail: weihuali@uow.edu.au and swzhang@ustc.edu.cn

Received 5 August 2016, revised 4 October 2016
Accepted for publication 2 November 2016
Published 18 November 2016

**Abstract**

Serving to improve stability and energy efficiency during locomotion, in nature, animals modulate their leg stiffness to adapt to their terrain. Now incorporated into many locomotive robot designs, such compliance control can enable disturbance rejection and improved transition between changing ground conditions. This paper presents a novel design of a variable stiffness leg utilizing a magnetorheological elastomer joint in a literal rolling spring loaded inverted pendulum (R-SLIP) morphology. Through the semi-active control of this hybrid permanent-magnet and coil design, variable stiffness is realized, offering a design which is capable of both softening and stiffening in an adaptive sort of way, with a maximum stiffness change of 48.0%. Experimental characterization first serves to assess the stiffness variation capacity of the torsional joint, and through later comparison with force testing of the leg, the linear stiffness is characterized with the R-SLIP-like behavior of the leg being demonstrated. Through the force relationships applied, a generalized relationship for determining linear stiffness based on joint rotation angle is also proposed, further aiding experimental validation.

Keywords: torsional MRE joint, variable stiffness, robotic leg, locomotion

(Some figures may appear in colour only in the online journal)

## 1. Introduction

Using their ligaments and tendons, running animals convert the gravitational potential and kinetic energy of their bodies into strain energy during leg compression, subsequently returned in the later-half of each step [1]. Considering the cyclic nature of this locomotion, animals of all sizes behave similar to spring-mass systems with their stride frequencies relating to both their body mass and the effective series stiffness made between their bodies and the terrain upon which they run [2, 3]. The dynamic behavior as described here is effectively modeled by the spring loaded inverted pendulum (SLIP) model, proposed by Blickhan in 1989 to describe human locomotion [4]. This important link between ground compliance, leg compliance, and stride frequency suggests optimal tuning of leg stiffness to suit a given terrain condition could lead to resonant, energy efficient locomotion [5]. In both humans and animals alike, it has been shown that as a means of maintaining gait stability and minimizing disturbance to center-of-mass trajectory during locomotion, leg stiffness modulation is utilized [3, 6, 7].

Since the birth of Raibert's hoppers with compliant legs [8], many legged robot platforms have been developed with compliant legs to achieve similar dynamic stability, such as Scout [9], RHex [10], and Sprawlita [11]. More recently, to incorporate some means of leg stiffness control to facilitate optimal tuning for energy efficient and stable locomotion, more research focus has been placed on the development of variable stiffness in legs. One example of which is the worm-gear driven slider mechanism in the C-shaped legs developed

[4] Author to whom any correspondence should be addressed.

 

by Galloway *et al* [12], providing a structural means of compliance control. L-MESTRAN (Linear MEchanism for varying Stiffness via Transmission Angle) developed by Vu *et al* [13] also utilizes the self-locking benefit of a worm-gear drive in a mechanism facilitating leg stiffness variation. In both of these cases, there exists a similar requirement of tuning time for the mechanisms to adjust the legs to a set-point stiffness. It is within this tuning time requirement that exists the potential to improve leg responsiveness to enable more rapid adaptation to changing ground conditions.

Magnetorheological elastomer (MRE) is a smart kind of material belonging to the MR family which possesses the ability to rapidly change its stiffness under the application of a magnetic field [14]. Typically, MRE is composed of a non-magnetic rubber host material such as silicone rubber, with suspended micro-scale ferromagnetic particles, wherein some additives may also be present, such as silicone oil [15]. When the material is brought into proximity with a magnetic field, it responds by stiffening as the evenly dispersed or pre-aligned chains of iron particles align to the field lines of the permanent magnet or electromagnet, this being the MR effect. Such a material can facilitate stiffness variation through a means of semi-active control.

In the past, devices or structures applied to the areas of dynamics, noise, or vibration have used either passively tuned components or have incorporated some form of active control with actuators to provide forcing [16]. Between these two cases, passive tuned devices usually represent reliable systems that lack versatility, while active controlled devices are typically more versatile, while sometimes lacking robustness and consuming large amounts of energy. On the other hand, to potentially improve energy efficiency while offering robustness closer to passively tuned devices in similar designs, semi-active materials such as MREs may be considered. It is for this reason that MRE has been widely used in adaptive-tuned-vibration absorbers [17–22], as well as other devices benefitting from controllable stiffness. On the far end of the spectrum in terms of stiffness variation capability, Li *et al* [15] designed a vibration isolator using MRE in a laminated structure capable of an increase in stiffness of up to 1630%.

In this paper, a variable stiffness leg taking the literal rolling spring loaded inverted pendulum (R-SLIP) [23] morphology, utilizing MRE in a variable stiffness joint, is designed and presented. The torsional spring of the model that typically represents an approximation of the compliant C-shaped leg stiffness is replaced with a torsional joint with a hybrid permanent magnet and electromagnet MRE-centered structure, providing a variable torsional stiffness. The relatively simple design significantly reduces the control effort to vary leg stiffness, achieved through adjusting the current level supplied to the coil. Owing to this and the favorable characteristics of the semi-active material, MRE has the potential to lead to similar advantageous performance in robot locomotion, offering greater energy efficiency or a lower cost-of-transport (CoT) and disturbance rejection through rapid stiffness tunability. It has been reported that MRE-based devices facilitating stiffness variation can adjust to a set-point stiffness as low as 1 ms [24]. The torsional MRE joint of the leg presented in this work should be no exception, with a similarly rapid response. Regarding the application of MRE to the field of locomotive robots, the prototype developed here represents the first reported case of MRE being applied to facilitate stiffness variation of limbs.

Following this introduction, the remainder of this paper is organized as follows. Section 2 details the structure and design process of the variable stiffness leg and leg joint. Section 3 includes the experimental characterization of both the rotary MRE joint and assembled variable stiffness leg, followed by the application of R-SLIP force relationships to describe leg behavior. Lastly, conclusions along with the potential for future work are discussed in section 4.

## 2. Design of the MRE-based leg

### 2.1. Leg structure

The concept design of the R-SLIP-based variable stiffness leg is presented in figure 1. Following the C-shaped structure of robot legs now typical in hexapods [12], these legs incorporate the variable stiffness joint at a position 60° from the vertical: being approximately near where the effective torsional spring is placed for compliant C-shaped legs [23], also shown to offer optimal stability in theoretical analysis [25]. Housed in the lower leg section, the joint is placed on an 80 mm radius, connected to the upper leg section through supporting arms, the left of which being pinned on a bearing, while the right connects directly to the output of the MRE joint, through which the toque is transmitted. In terms of the materials used to fabricate the illustrated design, the leg sections and linkages are 3D printed for ease of manufacture with varied density 'honeycomb' structures to provide a good balance between strength, robustness and weight. The total weight of this leg is 912 g, which is far from some other similarly designed legs, such as the 85 g C-shaped variable stiffness legs of [12] which were coupled to the lightweight platform EduBot. Clearly these legs would not be suitable for the 3 kg platform, although alternative heavier platforms may be better equipped for the legs presented here.

Regarding what relationships are applicable to both design and characterization of this leg, these are provided by Huang *et al* [23], the creators of the R-SLIP model. What is offered in this work is a relationship developed to relate the torsional stiffness of the model to an equivalent linear stiffness, serving to facilitate a comparison between the R-SLIP and SLIP models. This has also subsequently proven to be useful in experimental characterization of C-shaped legs [26, 27]. The relationship is based on the leg geometry, and the so-called $k_{10\%}$ rule, whereby a virtual linear spring placed inside the leg, compressed to 90% of its free-length, can be considered in determining a matched torsional stiffness. With the parameters of this relationship illustrated in figure 2, n.b. without the '10%' subscripts as a more general representation,

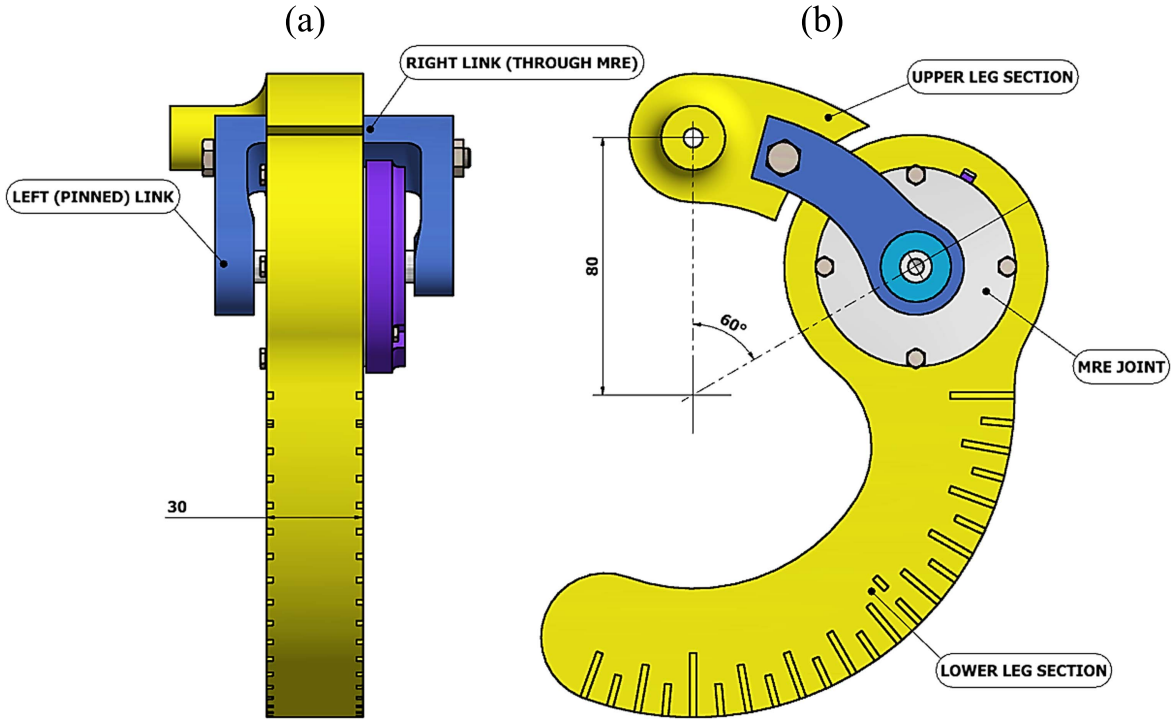


**Figure 1.** Structure of the variable stiffness leg; (a) back view, (b) side view.

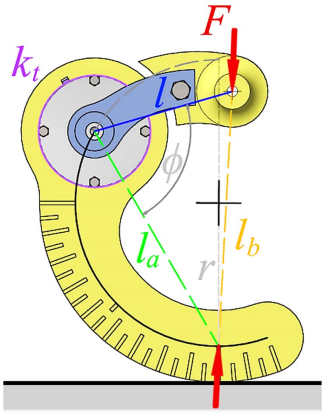


**Figure 2.** R-SLIP static model parameters.

the force model is formed by the following equations:

$$F_{10\%} = \frac{l_b k_t \left(\frac{\pi}{2} - \phi_{10\%}\right)}{(l)(l_a)\sin(\phi_{10\%})}, \tag{1}$$

and

$$\phi_{10\%} = \cos^{-1}\left(\frac{l^2 + l_a^2 - l_b^2}{2(l)(l_a)}\right), \tag{2}$$

where $l$ is the chord length drawn from the torsional joint to the loading point, the length of the chord drawn from the torsional joint to the contact point is $l_a = \sqrt{l_0^2 - l^2}$, with the free-length of the spring given by $l_0 = 2r$, and the spring length at 10% compression is $l_b = 0.9l_0$.

Then describing the leg by a linear spring at 10% compression, the stiffness $k_{10\%}$ is given by:

$$k_{10\%} = \frac{F_{10\%}}{0.1l_0}. \tag{3}$$

Considering the nature of this design with an actual torsional spring, the deflection angle of the spring can be readily measured in practice, making it more appropriate to base other parameters off this. Further, this facilitates ease of comparison between rotational and linear experimental data, as obtained in the testing of this variable stiffness leg. Suppose then the deflection angle of the joint is represented by $\psi$, the angle subtended by the loading point of the upper leg segment and the contact point of the lower leg segment $\phi$, is given by:

$$\phi = \phi_0 - \psi = \frac{\pi}{2} - \psi, \tag{4}$$

where $\phi_0$ is the initial angle formed, equal to $\pi/2$ for a 0° contact angle.

Assuming $\phi$ is now known, the compressed spring length $l_b$ can be determined from:

$$l_b = \sqrt{l^2 + l_a^2 - 2(l)(l_a)\cos(\phi)}. \tag{5}$$

To further generalize the force model for any reasonable deflection level, one last modification pertains to equation (3), where the deflection of the virtual linear spring $0.1l_0$ is

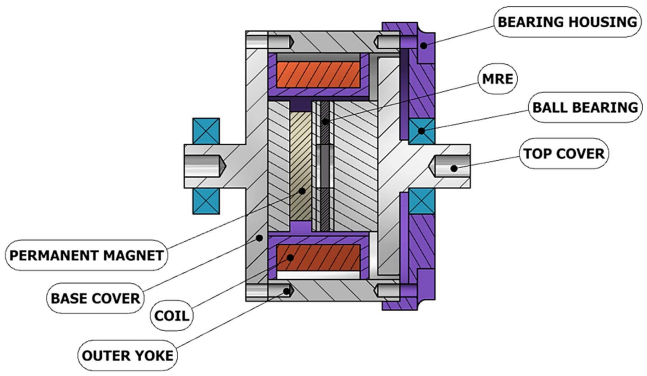


**Figure 3.** Variable stiffness torsional MRE joint.

replaced by $(l_0 - l_b)$, giving the last relationship:

$$k = \frac{F}{(l_0 - l_b)}. \tag{6}$$

Finally, based on a given torsional stiffness, torsional spring rotational deflection, and geometric properties, through the combination of equations (1), and (4) through (6), a matched equivalent linear stiffness can be obtained from equation (7):

$$k = \frac{l_b\left(\frac{\pi}{2} - \phi\right)}{(l_0 - l_b)(l)(l_a)\sin(\phi)} \times k_t. \tag{7}$$

This generalized relationship can serve as both a basis for design of a similar C-shaped leg following a literal R-SLIP morphology, and for analysis of rotational or linear test results of a leg-joint or leg design, respectively. Later discussed in this work is the application of this relationship to compare the experimental results of both the leg and leg joint, providing a means of validation of the test results and demonstrating R-SLIP-like behavior.

### *2.2. Design of the torsional MRE joint*

As for the main functional part of the design, the torsional MRE joint is illustrated with a sectional view in figure 3. The main parts of the joint consist of the MRE, the energizing electromagnetic coil, the permanent magnet, and the low-carbon steel magnetic circuit formed by the top and base covers and the outer yoke. When current is supplied to the coil, depending on the direction of current flow, this field will either add or subtract from the existing field produced by the permanent magnet, providing stiffening or softening respectively. Beyond these, the bearings and housing enable mounting within the additional parts of the leg. It should also be mentioned that the top cover serves as the torque output, while other parts of the joint such as the base cover and yoke are fixed to the lower section of the leg. Regarding the permanent magnet, this was implemented to enable plus-or-minus stiffness to broaden the controllability of the leg.

As for the MRE selected, this was fabricated with a mass ratio of carbonyl iron particles type C3518 (Sigma-Aldrich Pty. Ltd), silicone rubber (Selleys Pty. Ltd), and silicone oil (type 378364, Sigma-Aldrich Pty. Ltd) of 7:2:1, with a detailed fabrication process and magnetorheological properties being described in [28]. Also, given the minimal contribution of material near the axis of rotation of a cylinder to torsional stiffness $k_t$, for a given thickness of material, it is apparent that the most efficient use of material is placing away from the central axis. Hence, in experimental attempts to increase the flux density within the MRE to yield greater stiffness variation, a 10 mm core was removed, forming a hollow disc, with a thickness of 2.0 mm. Lastly, to bond the MRE with the other components of the core, super-glue adhesive (Selleys Pty. Ltd) was used.

In order to aid the design process of the joint, stationary magnetic field analysis was performed using COMSOL Multiphysics with a 2D axisymmetric field study. In terms of magnetic circuit design, the joint utilizes the basic concept of a ferrous-core surrounded by a solenoid with the flux path completed around the coil, through its covers and outer yoke. While some degree of flux leakage is always to be expected, the necessity of a gap in this circuit to allow relative motion between the input and output is an example of where this could not be avoided. As such, the clearance here was set to be 0.5 mm, as any less was assumed to have the potential induce friction if the joint was to deflect radially. Regarding the coil, a compromise between the joint geometry and required field strength led to a design of 400 turns.

As for the field simulation studies, with the results illustrated in figure 4; the steel was defined as 1020 low carbon steel, using the inbuilt B–H relationship; the magnet was defined as N30 grade neodymium with a relative permeability of 1.05 [29], possessing a remanant flux density of 1.08 T as per the properties of this grade of NdFeB; and the MRE was defined based on the B–H relationship provided by Xing *et al* in [30] for similarly fabricated 7:2:1 weight ratio MRE.

As illustrated in figure 4(a), the mean flux through the MRE ranges from 266 mT to 758 mT under currents of −3 A to 3 A respectively, i.e. adding to or taking away from the magnetization of the permanent magnet. While in general 600 mT is regarded as ideally the maximum flux in MRE [31] as saturation tends to occur around here [32], based on the B–H relationship utilized here, the degree to which this saturation deviates from a linear increase in flux with coercive force $H$ is not substantial as 800 mT is approached. Hence, this flux density appears acceptable.

## 3. Experimental characterization

To characterize the stiffness variation performance of the torsional joint and leg, the joint alone was first tested. Following this, the assembled leg was tested in a linear forcing arrangement, to evaluate its stiffness variation capability. Subsequent comparison between these test results provide validation of the testing methods and demonstrate the R-SLIP-like behavior of the leg, this being done through the application of the modified R-SLIP force relationships as provided in the previous section.

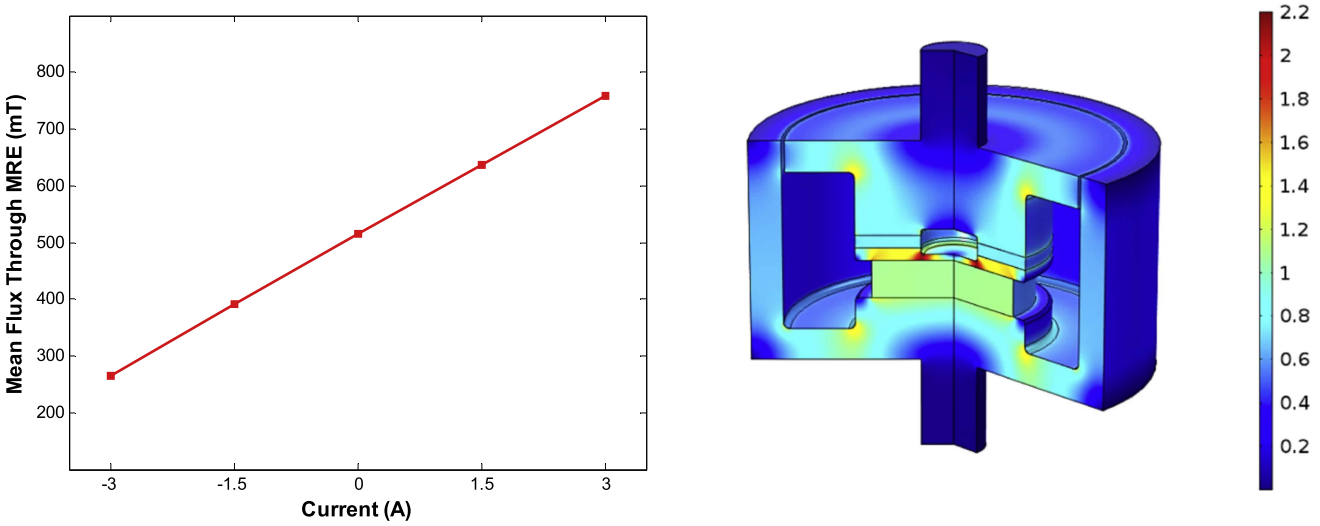


**Figure 4.** Magnetic field analysis results: (a) MRE flux and current relationship, (b) modeled joint.

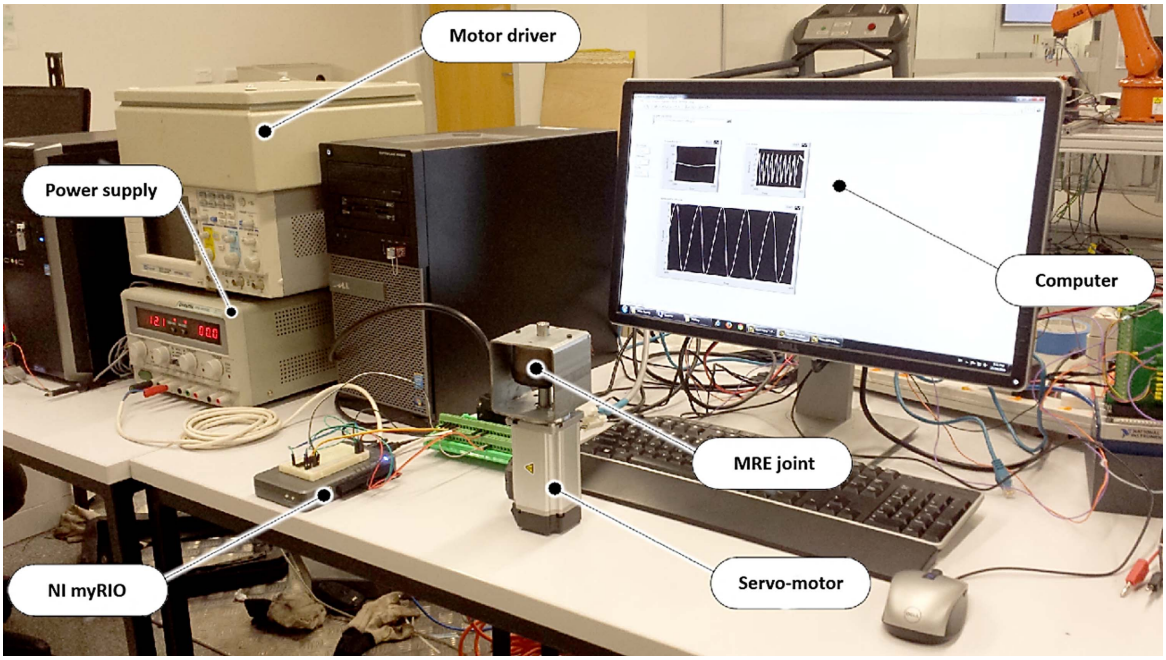


**Figure 5.** Experimental setup for torsional tests of the MRE joint.

### *3.1. Torque testing of the MRE joint*

Illustrated in figure 5, the torsional joint was tested through coupling it to a DC servo-motor and driver system (Panasonic 1.3 N m, MBDKT2510CA1 200 V), connected to an NI myRIO-1900, being the interface to a desktop computer running LabVIEW. The myRIO served as both the data acquisition (DAQ) board and a controller, supplying the motor driver with the angular position control signal, whilst recording the measured torque signal. The joint was loaded sinusoidally with a cosine signal, i.e. unidirectional loading, in order to more accurately replicate its behavior when deflected in the leg. During this time, through the use of a bench DC power supply (GW INSTEK GPC-3030D), the coil of the joint was supplied with different current levels, energizing the MRE.

Presented in figure 6, the results from this mode of testing at a frequency of 1 Hz, assumed to be a reasonable estimate of deflection rate during running, are included for deflection levels of 10° (figure 6(a)) and 20° (figure 6(b)). The hysteresis loops of these plots follow clockwise loading paths, illustrated by the arrows drawn on the figures. Based on these torque-displacement results, and given the harmonic loading of the MRE, the effective torsional stiffness $k_{t,eff}$ and equivalent viscous torsional damping $c_{t,eq}$ can be determined

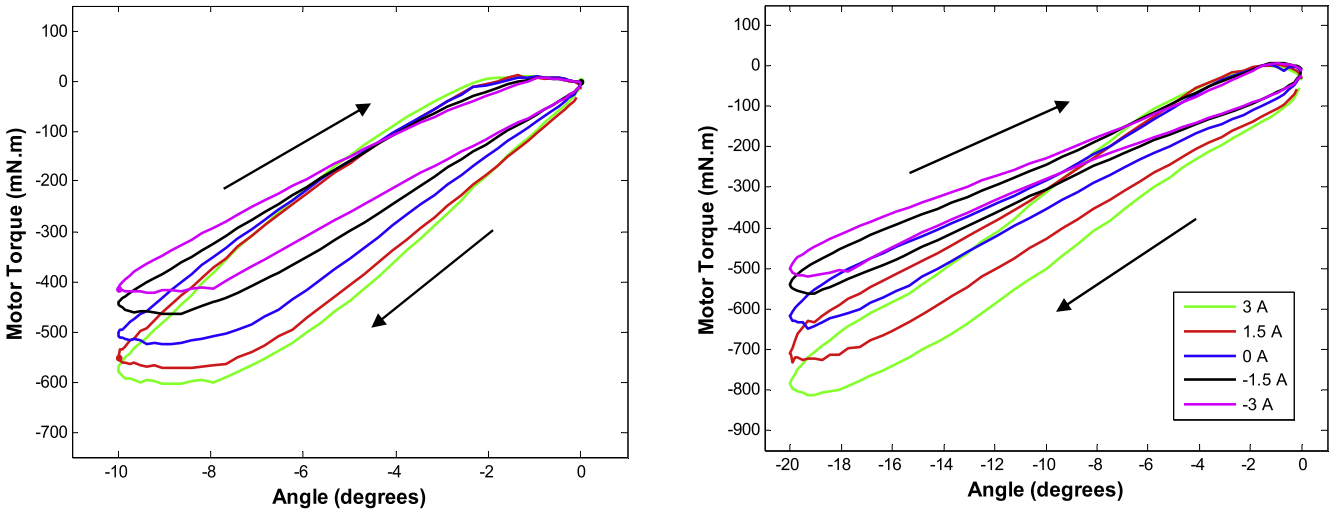


**Figure 6.** Torsional tests results at (a) 10°, and (b) 20° displacements.

**Table 1.** Effective torsional stiffness and torsional damping test results.

| | Applied current ($A$) | | | | | |
|---|---|---|---|---|---|---|
| Deflection level | −3.0 | −1.5 | 0.0 | 1.5 | 3.0 | Increase from −3.0 → 3.0 A (%) |
| | Effective torsional stiffness (N m rad$^{-1}$) | | | | | |
| 10° | 2.364 | 2.531 | 2.879 | 3.085 | 3.286 | 39.02 |
| 20° | 1.393 | 1.521 | 1.719 | 1.909 | 2.148 | 54.24 |
| | Equivalent torsional damping (N m s rad$^{-1}$) | | | | | |
| 10° | 0.109 | 0.128 | 0.168 | 0.209 | 0.235 | 114.56 |
| 20° | 0.040 | 0.042 | 0.048 | 0.067 | 0.093 | 135.23 |

using:

$$k_{\mathrm{t,eff}} = \frac{T_{\mathrm{d,max}} - T_{\mathrm{d,min}}}{\Delta_{\theta\mathrm{max}} - \Delta_{\theta\mathrm{min}}} \tag{8}$$

and

$$c_{\mathrm{t,eq}} = \frac{\mathrm{EDC}}{2\pi^2 f \Delta_\theta^2} \tag{9}$$

respectively, adapting the force–displacement equations used in [33]. Here, $T_{\mathrm{d,max}}$ and $T_{\mathrm{d,min}}$ represent the torque levels at the maximum and minimum angular deflections, $\Delta_{\theta\mathrm{max}}$ and $\Delta_{\theta\mathrm{min}}$ respectively. $\Delta_\theta$ is the corresponding sinusoid amplitude, i.e. $\Delta_{\theta\mathrm{min}}/2$ in this case, EDC is the energy dissipated per cycle, corresponding to the enclosed area of each loop, and $f$ is the loading frequency in Hz.

As included in table 1, it can be seen that for a 10° displacement, the maximum increase in torsional stiffness across the full current range tested is 39.02%, with a maximum stiffness of 3.286 N m rad$^{-1}$. For the 20° test, this increase was determined to be slightly greater at 54.24%, with a smaller maximum stiffness of 2.148 N m rad$^{-1}$. This behavior is consistent with the rheological behavior of MRE as reported by Li *et al* in [33]; in the vibration isolator design presented here, it was shown that in general for a larger strain amplitude, a lower stiffness, with a more substantial change over a tested current range occurs. Also, similar correlation is observed in that with greater displacement, a somewhat larger increase in equivalent damping was observed.

### *3.2. Force testing of the leg*

The experimental setup for this mode of testing is illustrated in figure 7. In this setup, the leg was affixed to the top clamp of the MTS Landmark hydraulic testing machine (Load Frame Model: 370.02, MTS Systems Corporation), where the lower section was free to slip on a low-friction acrylic base atop a load transducer. The servo-hydraulic actuator of the system supplied vertical loads in pre-programmed sinusoidal motions via the computer as the load, displacement, and time data was saved via a DAQ board. To energize the MRE joint of the leg, a bench DC power supply (CPX400 A, Aim-TTi Ltd) was used to supply current to the coil. In this instance, at 0° contact angle on the leg, i.e. in its up-right stance position, tests were conducted at varied currents in the MRE joint, later with different loading frequencies and displacement levels. Provided the torsional stiffness has already been experimentally determined, whereas typical C-shaped leg

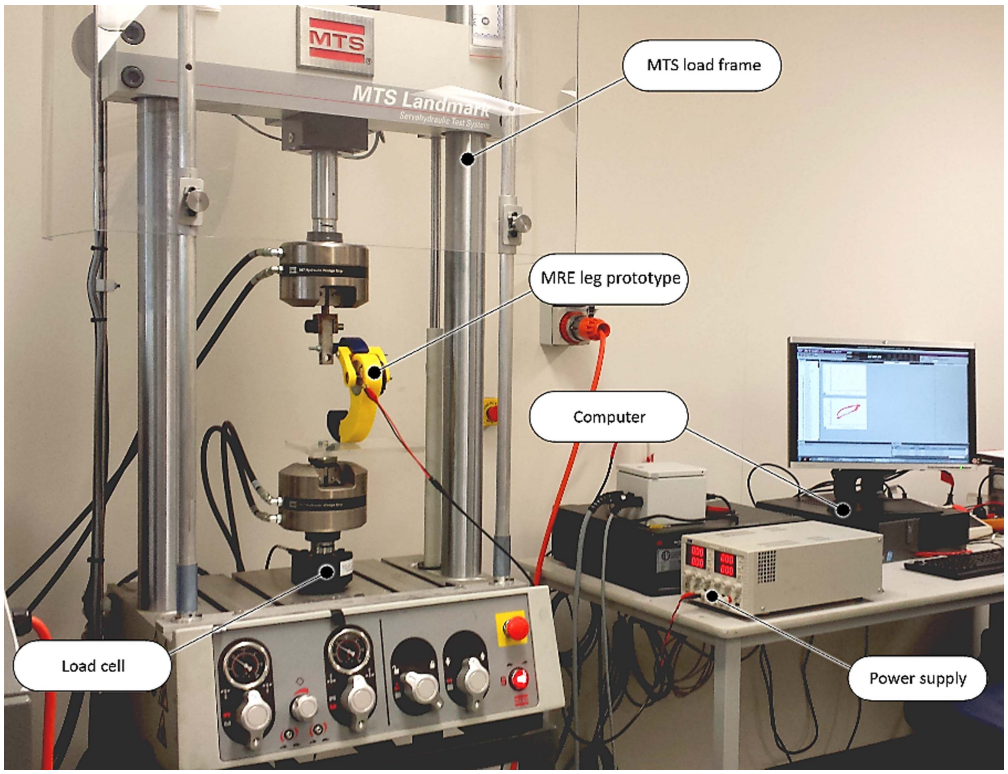


**Figure 7.** Experimental setup for linear tests of the variable stiffness leg.

characterization involves testing at multiple contact angles [26, 27], this is not necessary here.

Illustrated in figure 8 are the results of the harmonic loading for a current range of –3 to 3 A, at a displacement level of 13.85 mm with a 1 Hz loading frequency; the arrows of the figure illustrate the clockwise loading paths. It should be noted that the basis for the selection of this displacement level was to match the linear test results here with the previously determined torsional stiffnesses. Based on the simple geometric relationships describing the C-shaped legs, it was found that 13.85 mm results in 10° joint deflection, as previously tested. Considering the '$k_{10\%}$ rule' as mentioned previously, a point of interest here is that this deflection level approximately corresponds to a 10% deflection level.

Included for reference in table 2, and illustrated in figure 9 are the relationships between current and effective linear stiffness $k_{\text{eff}}$, and equivalent linear damping $c_{\text{eq}}$. Similar to in the torsional testing, equations (8) and (9) are again applied, albeit this time considering forces and linear displacements rather than torques and angular displacements.

As illustrated, at a current level of –3 A, the leg has an effective linear stiffness of 428.19 N m$^{-1}$, which after a maximum change of 48.01% becomes 633.78 N m$^{-1}$ under a 3 A current level. This range here is reasonable similar to that of the torsional tests, i.e. 39.02%, with deviation potentially due to the different nature of the loading and other, perhaps frictional, forces present. Given the near-linear relationship shown here, this essentially means a ±24% capability for stiffness variation about the median 0 A current stiffness of 547.1 N m$^{-1}$. It should also be noted that, given the nature of the rolling contact in these sort of legs, the effective vertical

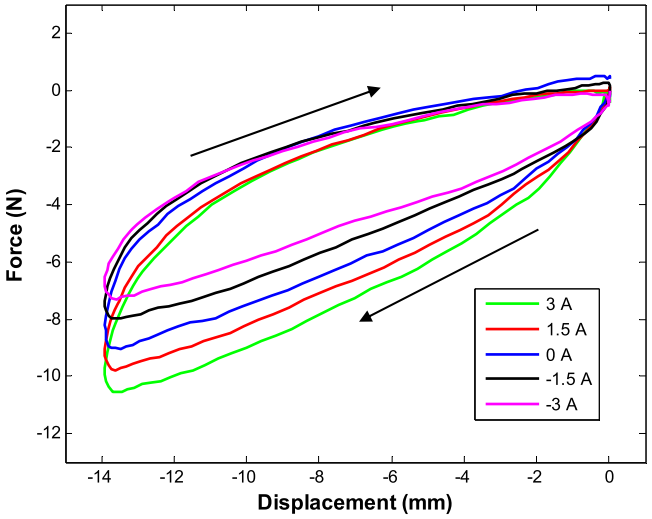


**Figure 8.** Stiffness variation of the leg under different current levels.

stiffness will increase as forward locomotion occurs due to the decreasing moment arm as the contact point approaches the torsional spring. What this means is there exists potential for widening this range through current control, or the converse: normalizing vertical stiffness through rolling contact to maintain an effective value. Both of these are again made possible due to the rapid response of MRE to an applied field.

In terms of damping, the measured force is shown to increase from 0.2737 N s m$^{-1}$ at a –3 A current level, to 0.4532 N s m$^{-1}$ at a 3 A current level, representing a 65.57% increase. Again, deviation from the torsional mode of testing here may be due to the difference between loading conditions,

**Table 2.** Effective linear stiffness and equivalent linear damping under different currents.

| | Applied current ($A$) | | | | | |
|---|---|---|---|---|---|---|
| | $-3.0$ | $-1.5$ | 0.0 | 1.5 | 3.0 | Increase from $-3.0 \rightarrow 3.0$ A (%) |
| $k_{\text{eff}}$ (N m$^{-1}$) | 428.19 | 481.05 | 547.1 | 588.76 | 633.78 | 48.01 |
| $c_{\text{eq}}$ (N s m$^{-1}$) | 0.2737 | 0.3320 | 0.3982 | 0.4062 | 0.4532 | 65.57 |

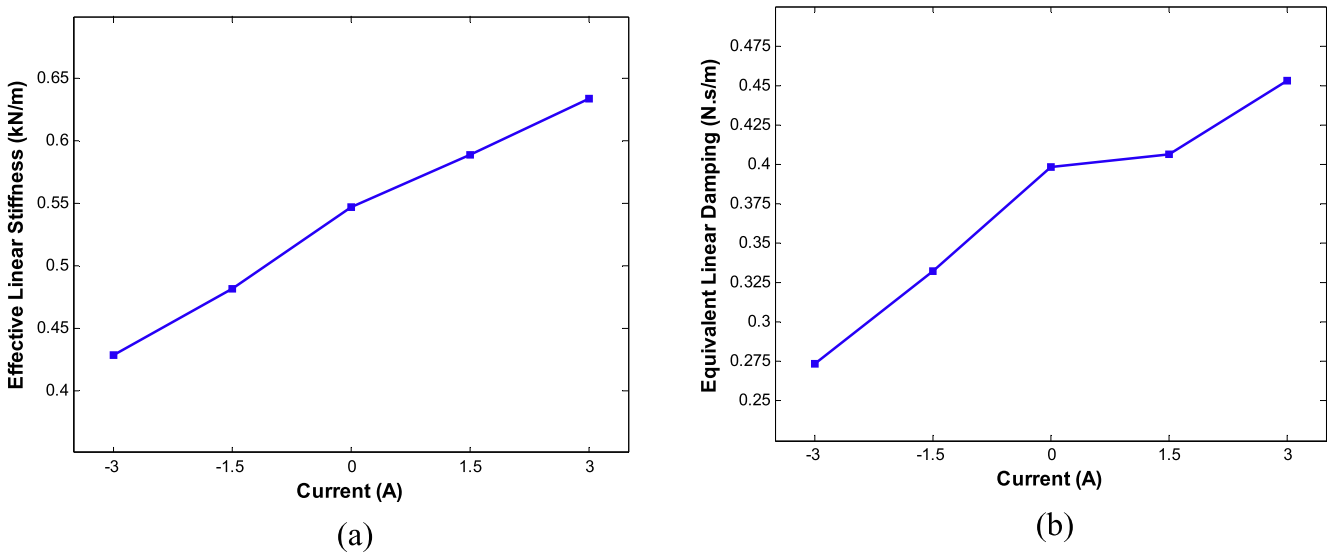


**Figure 9.** Relationship between current and (a) effective stiffness, (b) equivalent damping.

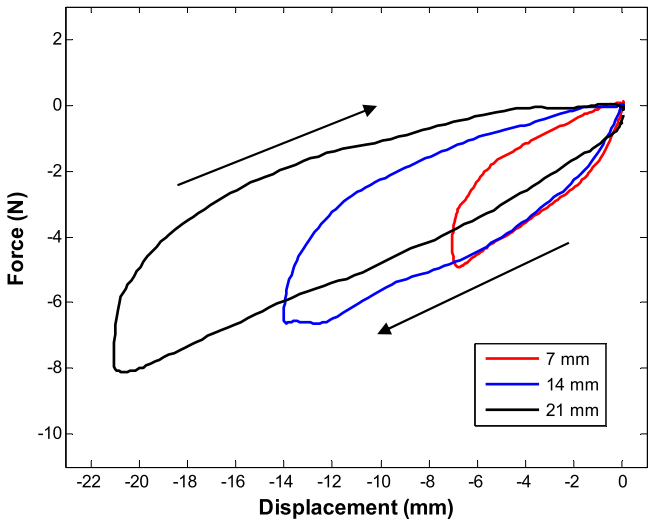


**Figure 10.** Leg behavior under different displacement levels.

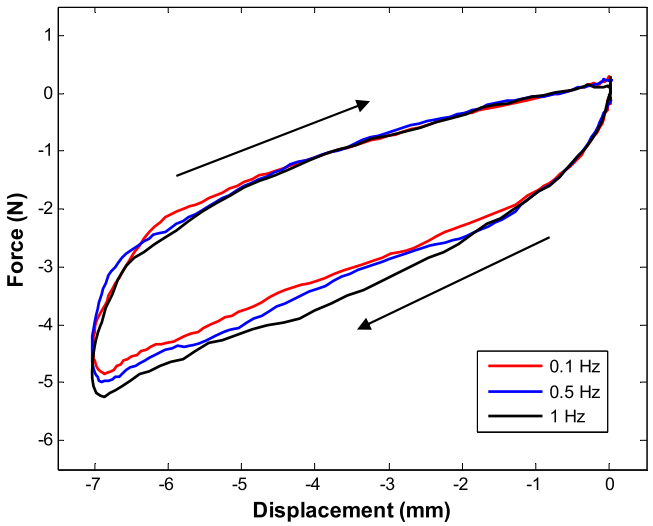


**Figure 11.** Leg behavior under different loading frequencies.

where in this case if more friction was present due to addition components, or through the sliding contact, the joint damping would have a relatively small role when compared to previous motor tests. Based on this, it would be quite reasonable to anticipate a smaller change in damping, due to the relatively small contribution of the MRE joint damping.

To further characterize the behavior of the leg, figure 10 shows the leg's performance for varied displacement levels (all at 0.5 Hz), and figure 11 shows its behavior under different loading frequencies (all at 7 mm amplitude). Again,

**Table 3.** Geometric data of the leg prototype.

| Parameter | Value |
|---|---|
| $l$ | 0.0800 m |
| $l_a$ | 0.1386 m |
| $l_b$ | 0.1475 m |
| $l_0$ | 0.1600 m |
| $\phi$ | 1.3964 rad |

**Table 4.** Numerical results from linear stiffness data comparison; stiffnesses in (N m$^{-1}$).

| | Applied current ($A$) | | | | | |
|---|---|---|---|---|---|---|
| | −3.0 | −1.5 | 0.0 | 1.5 | 3.0 | Increase from −3.0 → 3.0 A (%) |
| MTS tests | 428.19 | 481.05 | 547.1 | 588.76 | 633.78 | 48.01 |
| Motor tests | 444.43 | 476.44 | 542.36 | 581.90 | 619.57 | 39.41 |
| Motor ($k_{10\%}$) | 434.41 | 465.70 | 530.12 | 568.78 | 605.59 | 39.41 |

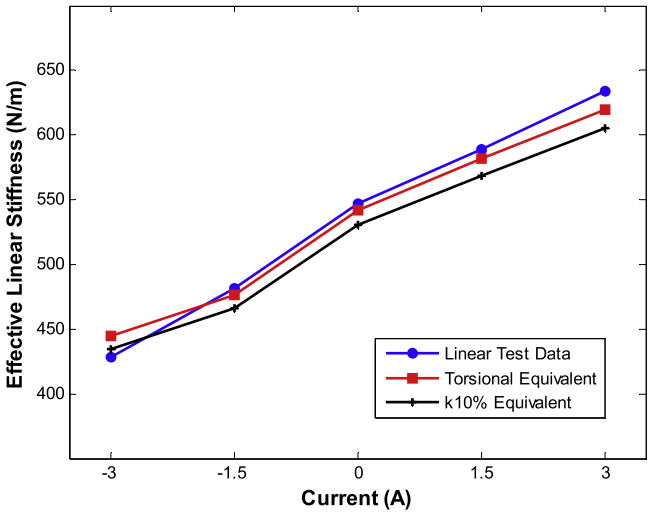


**Figure 12.** Matched linear stiffness data from torsional and linear testing.

these plots follow clockwise loading paths as illustrated by the arrows on the figures. As was the case in the torsional tests, consistent with the rheological behavior of MRE [33], in figure 10 it can be seen that as displacement amplitude increases, there is some degree of softening or decrease in stiffness. Similarly, as anticipated, in figure 11, a subtle increase in stiffness can be observed as loading frequency increases. It should be noted though that, given this change in stiffness for the tested frequency range is quite small, this demonstrates the leg's dynamic performance does not depend largely on loading frequency. This is useful for both practicality and making the results found here more universal.

### *3.3. Comparison of torsional and linear results*

Applying the generalized relationship between torsional stiffness and linear stiffness, as included in the design section, using the experimental data for effective torsional stiffnesses $k_{t,\text{eff}}$ at different current levels and 10° deflection, included in table 1, along with the geometric reference data of table 3, corresponding to the designed leg, the equivalent linear stiffnesses can be found. These are both listed in table 4, and illustrated in figure 12. Further, simply for the sake of comparison to what the $k_{10\%}$ rule would predict, given 10% compression is similar to 10° joint deflection for this leg, the equations in their original form are also applied. It can be seen that while in itself, this rule can predict the linear stiffness reasonably well with a mean error of 3.11%, the result is more accurate when the true deflection levels are considered, with a mean error of 1.79%.

Based on the good match between the force model used in R-SLIP analysis and the torsional test results, what now can be established is the leg is performing as intended in an R-SLIP-like manner, also offering a means of force-model validation, at least in terms of effective elastomer stiffness. Regarding the damping of the torsional joint, it should be noted that for the sake of R-SLIP based simulation and dynamic analysis, given this model considers the locomotion of the leg and platform mass to be a conservative system, it may be more appropriate to consider the non-conservative torque-actuated dissipative R-SLIP (TDR-SLIP) model, developed by Hu *et al* [34].

## 4. Conclusions

A variety of novel variable stiffness leg designs to improve upon gait performance have been developed over the past few years, striving to bring legged robots towards biological robustness and adaptability. Through experimentation, the adaptive leg presented here was demonstrated to possess a maximum stiffness shift of 48.0%. Further, the R-SLIP like behavior of the leg was demonstrated, through the application of the generalized relationship proposed, also providing validation between testing procedures. Regarding future work, later efforts will be placed in evaluating the leg's performance on a robot platform or locomotive test apparatus to explore the semi-active control approaches possible for this adaptive leg.

## Acknowledgments

This research is supported by Australian Research Council under Grant Nos. DP150102636 and LP150100040.

## References

[1] Dickinson M H, Farley C T, Full R J, Koehl M A R, Kram R and Lehman S 2000 How animals move: an integrative view *Science* **288** 100–6
[2] Heglund N C, Taylor C R and McMahon T A 1974 Scaling stride frequency and gait to animal size: mice to horses *Science* **186** 1112–3

[3] Farley C T, Houdijk H H P, Van Strien C and Louie M 1998 Mechanism of leg stiffness adjustment for hopping on surfaces of different stiffnesses *J. Appl. Physiol.* **85** 1044–55
[4] Blickhan R 1989 The spring-mass model for running and hopping *J. Biomech.* **22** 1217–27
[5] Alexander R M 1990 Three uses for springs in legged locomotion *Int. J. Robot. Res.* **9** 53–61
[6] Clark B D 1988 Mechanics and control on the hind limb of bobwhite quail running and landing on substrates of unpredictable mechanical stiffness *PhD Thesis* (University of Chicago, Department of Anatomy)
[7] Ferris D P, Louie M and Farley C T 1998 Running in the real world: adjusting leg stiffness for different surfaces *Proc. R. Soc.* B **265** 989–94
[8] Raibert M H 1986 *Legged Robots that Balance* (Cambridge, MA: Massachusetts Institute of Technology)
[9] Buehler M, Battaglia R, Cocosco A, Hawker G, Sarkis J and Yamazaki K 1998 SCOUT: a simple quadruped that walks, climbs, and runs *Proc. 1998 IEEE Int. Conf. on Robotics and Automation* pp 1707–12
[10] Saranli U, Buehler M and Koditschek D E 2001 RHex: a simple and highly mobile hexapod robot *Int. J. Robot. Res.* **20** 616–31
[11] Cham J G 2002 On performance and stability in open-loop running *PhD Thesis* (Stanford University)
[12] Galloway K C, Clark J E and Koditschek D E 2013 Variable stiffness legs for robust, efficient, and stable dynamic running *J. Mech. Robot.* **5** 011009
[13] Vu H Q 2013 A variable stiffness mechanism for improving energy efficiency of a planar single-legged hopping robot *16th Int. Conf. on Advanced Robotics (ICAR)* pp 1–7
[14] Chen L 2007 Microstructures and viscoelastic properties of anisotropic magnetorheological elastomers *Smart Mater. Struct.* **16** 2645–50
[15] Li Y, Li J, Tian T and Li W 2013 A highly adjustable magnetorheological elastomer base isolator for applications of real-time adaptive control *Smart Mater. Struct.* **22** 129501
[16] Dyke S J, Spencer B F Jr, Sain M K and Carlson J D 1996 Modeling and control of magnetorheological dampers for seismic response reduction *Smart Mater. Struct.* **5** 565–75
[17] Deng H X and Gong X L 2007 Adaptive tuned vibration absorber based on magnetorheological elastomer *J. Intell. Mater. Syst. Struct.* **18** 1205–10
[18] Hoang N, Zhang N and Du H 2009 A dynamic absorber with a soft magnetorheological elastomer for powertrain vibration suppression *Smart Mater. Struct.* **18** 074009
[19] Behrooz M, Wang X and Gordaninejad F 2014 Modeling of a new semi-active/passive magnetorheological elastomer isolator *Smart Mater. Struct.* **23** 045013
[20] Yang J *et al* 2016 Development of a novel multi-layer MRE isolator for suppression of building vibrations under seismic events *Mech. Syst. Signal Process.* **70–71** 811–20
[21] Sun S *et al* 2015 An adaptive tuned vibration absorber based on multilayered MR elastomers *Smart Mater. Struct.* **24** 045045
[22] Yang J, Sun S S, Du H, Li W H, Alici G and Deng H X 2014 A novel magnetorheological elastomer isolator with negative changing stiffness for vibration reduction *Smart Mater. Struct.* **23** 105023
[23] Huang K J, Huang C K and Lin P C 2014 A simple running model with rolling contact and its role as a template for dynamic locomotion on a hexapod robot *Bioinsp. Biomim.* **9** 046004
[24] Ginder J M, Nichols M E, Elie L D and Clark S M 2000 Controllable-stiffness components based on magnetorheological elastomers *Proc. SPIE* **3985** 418
[25] Huang C K and Lin P C 2015 Asymmetric stability property of a sagittal-plane model with a compliant leg and Rolling contact *Proc. 17th Int. Conf. on Advanced Robotics, ICAR 2015* pp 111–6
[26] Huang K-J, Chen S-C, Komsuoglu H, Lopes G, Clark J and Lin P-C 2015 Design and performance evaluation of a bio-inspired and single-motor-driven hexapod robot with dynamical gaits *J. Mech. Robot.* **7** 031017
[27] Chou Y-C, Huang K-J, Yu W-S and Lin P-C 2015 Model-based development of leaping in a hexapod robot *IEEE Trans. Robot.* **31** 40–54
[28] Hu G 2011 Experimental investigation of the vibration characteristics of a magnetorheological elastomer sandwich beam under non-homogeneous small magnetic fields *Smart Mater. Struct.* **20** 127001
[29] Kremers M F, Paulides J J, Ilhan E, Janssen J L and Lomonova E A 2013 Relative permeability in a 3D analytical surface charge model of permanent magnets *IEEE Trans. Magn.* **49** 2299–302
[30] Xing Z W, Yu M, Fu J, Wang Y and Zhao L J 2015 A laminated magnetorheological elastomer bearing prototype for seismic mitigation of bridge superstructures *J. Intell. Mater. Syst. Struct.* **26** 1818–25
[31] Xing Z 2016 A hybrid magnetorheological elastomer-fluid (MRE-F) isolation mount: development and experimental validation *Smart Mater. Struct.* **25** 015026
[32] Yang C Y, Fu J, Yu M, Zheng X and Ju B X 2015 A new magnetorheological elastomer isolator in shear-compression mixed mode *J. Intell. Mater. Syst. Struct.* **26** 1290–300
[33] Li Y, Li J, Li W and Samali B 2013 Development and characterization of a magnetorheological elastomer based adaptive seismic isolator *Smart Mater. Struct.* **22** 035005
[34] Hu C J, Huang C K and Lin P C 2015 A torque-actuated dissipative spring loaded inverted pendulum model with rolling contact and its use as the template for design and dynamic behavior generation on a hexapod robot *Proc. IEEE Int. Conf. on Robotics and Automation* pp 5177–83